

1 **Tropopause Evolution in a Rapidly Intensifying Tropical Cyclone: A Static**
2 **Stability Budget Analysis in an Idealized, Axisymmetric Framework**

3 Patrick Duran* and John Molinari

4 *University at Albany, State University of New York, Albany, NY*

5 **Corresponding author address:* Department of Atmospheric and Environmental Sciences, Univer-
6 sity at Albany, State University of New York, 1400 Washington Avenue, Albany, NY.

7 E-mail: pduran2008@gmail.com

ABSTRACT

8 Large changes in tropopause-layer static stability are observed during the
9 rapid intensification (RI) of an idealized, axisymmetric tropical cyclone (TC).
10 Over the eye, static stability near the tropopause decreases and the cold-point
11 tropopause height rises by up to 4 km at the storm center. Outside of the eye,
12 static stability increases considerably just above the cold-point tropopause,
13 and the tropopause remains near its initial level.

14 A budget analysis reveals that advection contributes to the static stability
15 tendencies at all times throughout the upper troposphere and lower strato-
16 sphere. Differential advection is particularly important within the eye, where
17 it acts to destabilize the layer near and above the cold-point tropopause.
18 Outside of the eye, a radial-vertical circulation develops during RI, with
19 strong outflow below the tropopause and weak inflow above. Vertical wind
20 shear above and below the upper-tropospheric outflow maximum induces tur-
21 bulence, which provides forcing for both destabilization and stabilization
22 in the tropopause layer. Meanwhile, as organized convection reaches the
23 tropopause, radiative heating tendencies at the top of the cirrus canopy gen-
24 erally act to destabilize the upper troposphere and stabilize the lower strato-
25 sphere. Turbulent mixing and radiative heating combine to play an important
26 role in the development of the strong stable layer immediately above the cold-
27 point tropopause during RI. The results suggest that turbulence and radiation,
28 alongside advection, play fundamental roles in the upper-level static stability
29 evolution of TCs.

30 **1. Introduction**

31 Using a high-resolution dropsonde dataset collected during the Tropical Cyclone Intensity ex-
32 periment (TCI; Doyle et al. 2017), Duran and Molinari (2018) observed dramatic changes in
33 tropopause structure during the rapid intensification (RI) of Hurricane Patricia (2015). The goal of
34 the present paper is to analyze the processes that might have produced the upper-tropospheric and
35 lower-stratospheric fluctuations observed in Patricia using an idealized axisymmetric simulation.

36 After undergoing a remarkably rapid intensification (RI), Hurricane Patricia (2015) set a new
37 record as the strongest tropical cyclone (TC) ever observed in the Western Hemisphere (Kimber-
38 lain et al. 2016; Rogers et al. 2017). TCI dropsonde observations collected during this RI period
39 revealed dramatic changes in the cold-point tropopause height and upper-level static stability (Du-
40 ran and Molinari 2018). In particular, when Patricia was at tropical storm intensity shortly before
41 RI commenced, a strong inversion layer existed just above the cold-point tropopause. During the
42 first half of the RI period, this inversion layer weakened throughout Patricia’s inner core, with the
43 weakening most pronounced over the developing eye. By the time the storm reached its maximum
44 intensity of 95 m s^{-1} , the inversion layer over the eye had disappeared almost completely, which
45 was accompanied by a greater than 1-km increase in the tropopause height. Meanwhile over the
46 eyewall region, the static stability increased and the tropopause remained near its initial level.

47 Despite the importance of tropopause-layer thermodynamics in theoretical models of hurri-
48 canes (Emanuel and Rotunno 2011; Emanuel 2012), most observational studies of the upper-
49 tropospheric structure of TCs are decades old. Recently, however, Komaromi and Doyle (2017)
50 found that stronger TCs tended to have a higher and warmer tropopause over their inner core than
51 weaker TCs. Their results are consistent with the evolution observed over the inner core of Hur-

52 ricane Patricia, in which the tropopause height increased and the tropopause temperature warmed
53 throughout RI (Duran and Molinari 2018).

54 Idealized simulations of a TC analyzed by Ohno and Satoh (2015) suggested that the develop-
55 ment of an upper-level warm core near the 13-km level acted to decrease the static stability near the
56 tropopause within the eye (compare their Figs. 9,10). Although the mechanisms that might drive
57 this static stability evolution have not been examined explicitly, Stern and Zhang (2013) described
58 the development of the TC warm core using a potential temperature (θ) budget analysis. They
59 found that radial and vertical advection both played important roles in warm core development
60 throughout RI, and subgrid-scale diffusion became particularly important during the later stage of
61 RI. To our knowledge, the only paper that has examined explicitly the static stability evolution in
62 a modeled TC is Kepert et al. (2016), but their analysis was limited to the boundary layer. The
63 analysis herein is based upon that of Stern and Zhang (2013), except using a static stability budget
64 similar to that of Kepert et al. (2016), with a focus on the upper troposphere and lower stratosphere.

65 **2. Model Setup**

66 The numerical simulations were performed using version 19.4 of Cloud Model 1 (CM1) de-
67 scribed in Bryan and Rotunno (2009). The equations of motion were integrated on a 3000-km-
68 wide, 30-km-deep axisymmetric grid with 1-km horizontal and 250-m vertical grid spacing. The
69 computations were performed on an f -plane at 15°N latitude, over a sea surface with constant
70 temperature of 30.5°C, which matches that observed near Hurricane Patricia (2015; Kimberlain
71 et al. 2016). Horizontal turbulence was parameterized using the Smagorinsky scheme described
72 in Bryan and Rotunno (2009, pg. 1773), with a prescribed mixing length that varied linearly from
73 100 m at a surface pressure of 1015 hPa to 1000 m at a surface pressure of 900 hPa. Vertical
74 turbulence was parameterized using the formulation of Markowski and Bryan (2016, their Eq. 6),

75 using an asymptotic vertical mixing length of 100 m. A Rayleigh damping layer was applied out-
76 side of the 2900-km radius and above the 25-km level to prevent spurious gravity wave reflection
77 at the model boundaries. Microphysical processes were parameterized using the Thompson et al.
78 (2004) scheme and radiative heating tendencies were computed every two minutes using the Rapid
79 Radiative Transfer Model for GCMs (RRTMG) longwave and shortwave schemes (Iacono et al.
80 2008). The initial temperature and humidity field was horizontally homogeneous and determined
81 by averaging all Climate Forecast System Reanalysis (CFSR) grid points within 100 km of Pa-
82 tricia's center of circulation at 18 UTC 21 October 2015. The vortex described in Rotunno and
83 Emanuel (1987, their Eq. 37) was used to initialize the wind field, setting all parameters equal to
84 the values used therein.

85 Although hurricanes simulated in an axisymmetric framework tend to be more intense than
86 those observed in nature, the intensity evolution of this simulation matches reasonably well with
87 that observed in Hurricane Patricia. After an initial spin-up period of about 20 hours, the modeled
88 storm (Fig. 1, blue lines) began an RI period that lasted approximately 30 hours. After this RI,
89 the storm continued to intensify more slowly until the maximum 10-m wind speed reached 89
90 m s^{-1} and the sea-level pressure reached its minimum of 846 hPa, 81 hours into the simulation.
91 Hurricane Patricia (red stars) exhibited a similar intensity evolution prior to its landfall, with an RI
92 period leading to a maximum 10-m wind speed of 95 m s^{-1} and a minimum sea-level pressure of
93 872 hPa.

94 3. Budget Computation

95 The static stability can be expressed as the squared Brunt-Väisälä frequency:

$$N_m^2 = \frac{g}{T} \left(\frac{\partial T}{\partial z} + \Gamma_m \right) \left(1 + \frac{T}{R_d/R_v + q_s} \frac{\partial q_s}{\partial T} \right) - \frac{g}{1 + q_t} \frac{\partial q_t}{\partial z}, \quad (1)$$

96 where g is gravitational acceleration, T is temperature, R_d and R_v are the gas constants of dry air
 97 and water vapor, respectively, q_s is the saturation mixing ratio, q_t is the total condensate mixing
 98 ratio, and Γ_m is the moist-adiabatic lapse rate:

$$\Gamma_m = g(1 + q_t) \left(\frac{1 + L_v q_s / R_d T}{c_{pm} + L_v \partial q_s / \partial T} \right), \quad (2)$$

99 where L_v is the latent heat of vaporization and c_{pm} is the specific heat of moist air at constant
 100 pressure. In the tropopause layer, q_s , $\partial q_s / \partial T$, and $\partial q_t / \partial z$ approach zero. In this limiting case,
 101 Eq. 1 reduces to:

$$N^2 = \frac{g}{\theta} \frac{\partial \theta}{\partial z}, \quad (3)$$

102 where θ is the potential temperature.

103 To compute N^2 , CM1 uses Eq. 1 in saturated environments and Eq. 3 in sub-saturated environ-
 104 ments. For simplicity, however, only Eq. 3 will be employed for the budget computations¹.

105 Taking the time derivative of Eq. 3 yields the static stability tendency:

$$\frac{\partial N^2}{\partial t} = \frac{g}{\theta} \frac{\partial}{\partial z} \frac{\partial \theta}{\partial t} - \frac{g}{\theta^2} \frac{\partial \theta}{\partial z} \frac{\partial \theta}{\partial t}, \quad (4)$$

106 where the potential temperature tendency, $\partial \theta / \partial t$, can be written, following Bryan (cited 2018):

$$\frac{\partial \theta}{\partial t} = -u \frac{\partial \theta}{\partial r} - w \frac{\partial \theta}{\partial z} + HTURB + VTURB + MP + RAD + DISS \quad (5)$$

107 Each term on the right-hand side of Eq. 5 represents a θ budget variable, each of which is output
 108 directly by the model every minute. Since the first term on the right-hand side of Eq. 4 is larger
 109 than the second term throughout most of the tropopause layer (not shown), the contribution of
 110 each of the terms in Eq. 5 to the N^2 tendency can be interpreted in light of a vertical gradient of
 111 each term.

¹The validity of this approximation will be substantiated later in this section.

Taking the vertical gradient of the first two terms on the right-hand side of Eq. 5 yields the time tendency of the vertical θ gradient due to horizontal and vertical advection²:

$$\left(\frac{\partial}{\partial t} \frac{\partial \theta}{\partial z}\right)_{adv} = -u \frac{\partial}{\partial r} \frac{\partial \theta}{\partial z} - w \frac{\partial}{\partial z} \frac{\partial \theta}{\partial z} - \frac{\partial u}{\partial z} \frac{\partial \theta}{\partial r} - \frac{\partial w}{\partial z} \frac{\partial \theta}{\partial z}. \quad (6)$$

The first two terms on the right-hand side of Eq. 6 represent advection of static stability by the radial and vertical wind, respectively. These terms act to rearrange the static stability field, but cannot strengthen or weaken static stability maxima or minima. The third and fourth terms on the right-hand side of Eq. 6 represent, respectively, the tilting of isentropes in the presence of vertical wind shear, and the stretching or squashing of isentropes by vertical gradients of vertical velocity. Since these terms involve velocity gradients, they can act to strengthen or weaken static stability maxima or minima through differential advection. For example, since the θ of the air flowing out of the eyewall into the upper-tropospheric outflow layer increases as the TC intensifies, θ increases locally within the outflow layer. This acts to increase $\partial\theta/\partial z$ below the outflow maximum and decrease $\partial\theta/\partial z$ above, thereby modifying the static stability field. Similarly, the decay of updrafts with height at the top of convective towers can act to increase $\partial\theta/\partial z$ through squashing of isentropes.

Returning to Eq. 5, HTURB and VTURB are the θ tendencies from the horizontal and vertical turbulence parameterizations, MP is the tendency from the microphysics scheme, RAD is the tendency from the radiation scheme, and DISS is the tendency due to turbulent dissipation. This equation neglects Rayleigh damping, since the entire analysis domain lies outside of the regions where damping is applied. Each term in Eq. 5 is substituted for $\partial\theta/\partial t$ in Eq. 4, yielding the contribution of each budget term to the static stability tendency. These terms are summed, yielding

²These terms include the tendencies due to implicit diffusion in the fifth-order finite differencing scheme, which are separated from the advection terms in the CM1 budget output

an instantaneous "budget change" in N^2 every minute. The budget changes are then averaged over 24-hour periods and compared to the total model change in N^2 over that same time period, i.e.:

$$\Delta N_{budget}^2 = \frac{1}{\delta t} \sum_{t=t_0}^{t_0+\delta t} \frac{\partial N^2}{\partial t} \bigg|_t \quad (7)$$

$$\Delta N_{model}^2 = N_{t_0+\delta t}^2 - N_{t_0}^2 \quad (8)$$

$$Residual = \Delta N_{model}^2 - \Delta N_{budget}^2 \quad (9)$$

where t_0 is an initial time and δt is 24 hours.

Eqs. 7-9 are plotted for three consecutive 24-hour periods in Fig. 2. For this and all subsequent radial-vertical cross sections, a 1-2-1 smoother is applied once in the radial direction to eliminate $2\Delta r$ noise that appears in some of the raw model output and calculated fields. The left column of Fig. 2 depicts the model changes computed using Eq. 8, together with Eq. 1 in saturated environments and Eq. 3 in subsaturated environments. The center column depicts the budget changes computed using Eq. 7 together with Eq. 3 throughout the entire domain. Thus, the left column includes the effect of moisture in the N^2 computations, whereas the center column neglects moisture. The right column depicts the residuals, computed using Eq. 9 (i.e. the left column minus the center column.) In every 24-hour period, the budget changes are nearly identical to the model changes, which is reflected in the near-zero residuals in the right column. This indicates that the budget accurately represents the model variability, which implies that the neglect of moisture in the budget computation introduces negligible error within the analysis domain³.

In the tropopause layer, some of the budget terms are small enough to be ignored. To determine which of the budget terms are most important, a time series of the contribution of each of the budget terms in Eq. 5 to the tropopause-layer static stability tendency is plotted in Fig. 3. For this

³This is not the case in the lower- and mid-troposphere, where the residual actually exceeds the budget tendencies in many places, likely due to the neglect of moisture; thus we limit this analysis to the upper troposphere and lower stratosphere.

figure, each of the budget terms is computed using the method described in Section 3, except with 1-hour averaging intervals instead of 24-hour intervals. The absolute values of these tendencies are then averaged over the radius-height domain of the plots shown in Fig. 2 and plotted as a time series⁴. Advection (Fig. 3, red line) plays an important role in the mean tropopause-layer static stability tendency at all times, and vertical turbulence (Fig. 3, blue line) and radiation (Fig. 3, dark green line) also contribute significantly. The remaining three processes - horizontal turbulence, microphysics, and dissipative heating - are negligible everywhere outside of the eyewall, and do not play important roles in the mesoscale tropopause variability.

The preceding analysis indicates that, at all times, three budget terms dominate the tropopause-layer static stability tendency: advection, vertical turbulence, and radiation. Variations in the magnitude and spatial structure of these terms drive the static stability changes depicted in Fig. 2; subsequent sections will focus on these variations and what causes them.

4. Results

a. Static stability evolution

The average N^2 over the first day of the simulation (Fig. 4a) indicates the presence of a weak N^2 maximum just above the cold-point tropopause. Over the subsequent 24 hours, during the RI period, the N^2 within and above this layer decreased within the 25-km radius (Fig. 4b). This decreasing N^2 corresponded to an increase in the tropopause height within the developing eye, maximized at the storm center. Outside of the eye, meanwhile, the tropopause height decreased over the eyewall region (25-60-km radius) and increased only slightly outside of the 60-km ra-

⁴It will be seen in subsequent figures that each of the terms contributes both positively and negatively to the N^2 tendency within the analysis domain. Thus, taking an average over the domain tends to wash out the positive and negative contributions. To circumvent this problem, the absolute value of each of the terms is averaged.

172 dius. In this outer region, the N^2 maximum just above the tropopause strengthened during RI.
 173 These trends continued as the storm's intensity leveled off in the 48-72-hour period (Fig. 4c). The
 174 tropopause height increased to nearly 21 km at the storm center and sloped sharply downward to
 175 16.3 km on the inner edge of the eyewall, near the 30 km radius. Static stability outside of the eye,
 176 meanwhile, continued to increase just above the cold-point tropopause. This N^2 evolution closely
 177 follows that observed in Hurricane Patricia (2015; Duran and Molinari 2018, see their Fig. 4). The
 178 mechanisms that led to these N^2 changes will be investigated in the subsequent sections.

179 *b. Static stability budget analysis*

180 *(i) 0-24 hours*

181 The initial spin-up period was characterized by a steady increase of the maximum wind speed
 182 from 11 m s^{-1} to 22 m s^{-1} (Fig. 1a, blue line), an intensification rate that closely matched that of
 183 TC Patricia (Fig. 1a, red stars). The weakening of the lower-stratospheric N^2 maximum during
 184 this period is reflected in the total N^2 budget change over this time (Fig. 5a). The layer just above
 185 the cold-point tropopause was characterized by decreasing N^2 (purple shading), maximizing at the
 186 storm center. At and immediately below the tropopause, meanwhile, saw increasing N^2 during this
 187 time period. Although these tendencies extended out to the 200-km radius, they were particularly
 188 pronounced at innermost radii. A comparison of the contributions of advection (Fig. 5b), vertical
 189 turbulence (Fig. 5c), and radiation (Fig. 5d) reveals that advection was the primary driver of the
 190 N^2 tendency during this period, acting to stabilize near and just below the tropopause and destabi-
 191 lize above. Although vertical turbulence acted in opposition to advection (i.e. it acted to stabilize
 192 regions that advection acted to destabilize), the magnitude of the advective tendencies was larger,
 193 particularly at the innermost radii. The sum of advection and vertical turbulence (Fig. 5e) almost
 194 exactly replicated the static stability tendencies above the tropopause. Radiative tendencies, mean-

195 while, (Fig. 5d) acted to destabilize the layer below about 16 km and stabilize the layer between
196 16 and 17 km. The sum of advection, vertical turbulence, and radiation (Fig. 5f) reproduced the
197 total change in N^2 almost exactly.

198 *(ii) 24-48 hours*

199 During the RI period, the maximum wind speed increased from 22 m s^{-1} to 80 m s^{-1} . Over this
200 time, N^2 within the eye generally decreased above 16 km and increased below (Fig. 6a), with the
201 destabilization above 16 km maximizing near the level of the mean cold-point tropopause. These
202 tendencies at the innermost radii were driven almost entirely by advection (Fig. 6b). Vertical
203 turbulence (Fig. 6c) and radiation (Fig. 6d) contributed negligibly to the static stability tendencies
204 in this region.

205 Outside of the eye, the N^2 evolution exhibited alternating layers of positive and negative tenden-
206 cies. Near and above 18 km existed an upward-sloping region of decreasing N^2 that extended out
207 to the 180-km radius. In this region, neither vertical turbulence nor radiation exhibited negative N^2
208 tendencies; advection was the only forcing for this destabilization. Immediately below this layer,
209 just above the cold-point tropopause, was a region of increasing N^2 that sloped upward from 17 km
210 near the 30-km radius to just below 18 km outside of the 100-km radius. Advection and vertical
211 turbulence both contributed to this positive N^2 tendency, with advection playing an important role
212 below about 17.5 km and and turbulence playing an important role above. The sum of advection
213 and turbulence (Fig. 6e) reveals two discontinuous regions of increasing N^2 in the 17-18-km layer
214 rather than one contiguous region. The addition of radiation to these two terms, however, (Fig. 6f)
215 provides the link between these two regions, indicating that radiation also plays a role in strength-
216 ening the stable layer just above the tropopause. In the 16-17-km layer, just below the cold-point
217 tropopause, a horizontally-extensive layer of destabilization also was forced by a combination of

218 advection, vertical turbulence, and radiation. The sum of advection and vertical turbulence ac-
219 counts for only a portion of the decreasing N^2 in this layer, and actually indicates forcing for
220 stabilization near the 50-km radius and outside of the 130-km radius. Radiative tendencies over-
221 come this forcing for stabilization in both of these regions to produce the radially-extensive region
222 of destabilization observed just below the tropopause.

223 The sum of advection, vertical turbulence, and radiation (Fig. 6f) once again closely follows
224 the observed N^2 variability, except in the eyewall region, where the neglect of latent heating and
225 horizontal turbulence introduces some differences.

226 *(iii) 48-72 hours*

227 After the storm's maximum wind speed leveled off near 80 m s^{-1} , the magnitude of the static
228 stability tendencies within the eye decreased to near zero (Fig. 7a).

229 Outside of the eye, however, N^2 continued to decrease in the layer immediately surrounding the
230 tropopause. The sum of advection and vertical turbulence (Fig. 7e) indicates that the increase of
231 N^2 observed in the 17-18-km layer and inside of the 80-km radius cannot be attributed to these
232 processes, since the sum of these two terms provided forcing for destabilization. Instead, radiation
233 (Fig. 7d) provided the forcing for stabilization in this region. Outside of the 80-km radius, both
234 advection (Fig. 7b) and vertical turbulence (Fig. 7c) provided forcing for stabilization near and
235 just above the 18-km level. The sum of the two terms (Fig. 7e) indicates increasing N^2 near the
236 18-km level everywhere outside of the 80-km radius, but this stabilization is slightly weaker in
237 the 90-120-km radial band than the observed value. The addition of radiation (Fig. 7f) provided
238 the extra forcing for stabilization required to account for the observed increase in N^2 . Outside
239 of the 120-km radius, the region of radiative forcing for stabilization sloped downward, and the
240 increase in N^2 observed near 18 km can be explained entirely by a combination of advection and

vertical turbulence. The layer of decreasing N^2 observed near the tropopause was forced primarily by vertical turbulence and radiation. Within most of this region, advection provided strong forcing for stabilization, but this forcing was outweighed by the negative N^2 tendencies induced by a combination of vertical turbulence and radiation.

5. Discussion

a. The role of advection

Advection played an important role in the tropopause-layer N^2 evolution at all stages of intensification, but for brevity, this section will focus only on the RI (24-48-hour) period. To investigate the advective processes more closely, the individual contributions of horizontal and vertical advection during the RI period are shown in Fig. 8, along with the corresponding time-mean radial and vertical velocities and θ . The N^2 tendencies due to the two advective components (Fig. 8a,b) exhibited strong cancellation, consistent with flow that was nearly isentropic. There were, however, many regions in which flow crossed θ surfaces; this flow accounted for all non-zero N^2 tendencies due to advection previously seen in Fig. 6b.

During the RI period, strong radial and vertical circulations developed near the tropopause (Fig. 8c,d), which forced high-magnitude N^2 tendencies due to advection (Fig. 8a,b). A layer of strong outflow formed at and below the tropopause during this period, with the outflow maximum (dashed cyan line) curving from the 14-km level at the 50-km radius to just below the 16-km level outside of the 80-km radius (Fig. 8c). Notably, the N^2 tendency due to horizontal advection (Fig. 8a) tended to switch signs at this line, with stabilization below the outflow maximum and destabilization above. This is consistent with the outflow layer carrying air with increasingly large θ from the eyewall to large radii as the storm intensified. This increase in θ maximized near

the outflow maximum, which acted to decrease $\partial\theta/\partial z$ above the outflow maximum and increase it below. This mechanism is the same as that discussed in Trier and Sharman (2009), in which vertical wind shear in the outflow layer of a mesoscale convective system acted to modify the upper-tropospheric static stability through differential advection of isentropes.

Meanwhile in the lower stratosphere, a thin layer of $2\text{--}4\text{ m s}^{-1}$ inflow developed a few hundred meters above the tropopause, similar to that which was observed in Hurricane Patricia (2015; Duran and Molinari 2018) and in previous modeling studies (e.g. Ohno and Satoh 2015; Kieu et al. 2016). Since the isentropes in this layer sloped slightly upward with radius (i.e. $\partial\theta/\partial r < 0$), this inflow acted to import lower θ air from outer radii to inner radii. Since the negative θ tendencies maximized at the level of maximum inflow, the layer below the inflow maximum destabilized and the layer above stabilized (Fig. 8a).

Curiously, horizontal advection contributed to the N^2 tendency everywhere within the eye, even though the mean radial velocity there was near zero. Close examination of the model output revealed that these tendencies were forced by advective processes associated with inward-propagating waves. Although the radial velocity perturbations induced by these waves averaged out to zero, the advective tendencies forced by the radial velocity perturbations did not. Additionally, when these waves reached $r=0$, a dipole of vertical velocity resulted, with ascent above and descent below. For reasons that remain unclear, the regions of ascent were more persistent than the regions of descent, which resulted in the mean ascent observed near $r=0$ above 17 km in Fig. 8b.

Vertical advection also played an important role in the tropopause-layer static stability evolution. Within the eye, subsidence dominated below 17 km, while mean ascent existed near the storm center above 17 km. Although the magnitude of the subsidence was larger at lower altitudes, $\partial\theta/\partial z$ was smaller there. Because $\partial\theta/\partial z$ was smaller, the subsidence at lower levels could not accomplish as much warming as the subsidence at higher levels in the eye, consistent with the

287 results of Stern and Zhang (2013). As a result, vertical advection within the eye acted to stabilize
288 the layer below 16 km during RI.

289 Outside of the 27-km radius, ascent dominated the troposphere, while a 1.5-km-deep layer of
290 descent existed immediately above the tropopause. These regions of ascent and descent converged
291 just above the tropopause; this convergence acted to compact the isentropes in this layer and in-
292 crease the static stability. Above the lower-stratospheric subsidence maximum, meanwhile, verti-
293 cal advection acted to decrease N^2 . Below the tropopause, differential vertical advection increased
294 N^2 within the eyewall region and also at larger radii above the vertical velocity maximum at larger
295 radii. Outside of the eyewall and below the vertical velocity maximum, meanwhile, differential
296 vertical advection acted to decrease N^2 .

297 Comparing the N^2 tendencies forced by horizontal (Fig. 8a) and vertical (Fig. 8b) advection
298 to the total advective tendency seen in Fig. 6b reveals that horizontal advective tendencies domi-
299 nated the troposphere, while vertical advective tendencies dominated the layer near and above the
300 tropopause. Thus, tilting of isentropes in the vicinity of the upper-tropospheric outflow maximum
301 appears to be the most important process governing the N^2 tendency in the troposphere, whereas
302 convergence of vertical velocity appears to be the most important process near the tropopause.

303 *b. The role of radiation*

304 During the initial spin-up period (0-24 hours; Fig. 9a), convection was not deep enough to
305 deposit large quantities of ice near the tropopause and create a persistent cirrus canopy. Due to the
306 lack of ice particles, the radiative heating tendencies during this period (Fig. 9b) were relatively
307 small and confined to the region above a few particularly strong, although transient, convective
308 towers. During RI (24-48 hours), the eyewall updraft strengthened and a radially-extensive cirrus
309 canopy developed near the tropopause (Fig. 9c). The enhanced vertical gradient of ice mixing ratio

310 at the top of the cirrus canopy induced strong diurnal-mean radiative cooling near the tropopause
 311 (Fig. 9d). This cooling exceeded 0.6 K h^{-1} in some places and sloped downward from the lower
 312 stratosphere into the upper troposphere, following the top of the cirrus canopy. A small radiative
 313 warming maximum also appeared outside of the 140-km radius below this region of cooling. These
 314 results broadly agree with those of Bu et al. (2014; see their Fig. 11a), whose CM1 simulations
 315 produced a 0.3 K h^{-1} diurnally-averaged radiative cooling at the top of the cirrus canopy and
 316 radiative warming within the cloud that maximized near the 200-km radius. This broad region
 317 of radiative cooling acted to destabilize the layer below the cooling maximum and stabilize the
 318 layer above, which can be seen in Fig. 6d. The small area of net radiative heating outside of the
 319 140-km radius enhanced the destabilization above 16 km in this region and produced a thin layer
 320 of stabilization in the 15-16-km layer.

321 After the TC's RI period completed (48-72 hours), strong radiative cooling remained near the
 322 tropopause at inner radii (Fig. 9f), sloping downward with the top of the cirrus canopy to below
 323 the tropopause at outer radii. Cooling rates exceeded 1 K h^{-1} just above the tropopause between
 324 the 30- and 70-km radii. This value is more than three times the maximum cooling rate of 0.3 K h^{-1}
 325 observed by Bu et al. (2014), a discrepancy that is a consequence of their larger vertical grid
 326 spacing compared to that used here, along with a contribution from differing radiation schemes. To
 327 compare our results to those of Bu et al. (2014), we ran a simulation identical to that described in
 328 Section 2, except using the NASA-Goddard radiation scheme and 625-m vertical grid spacing, to
 329 match those of Bu et al. (2014). This simulation produced a maximum 24-hour-average radiative
 330 cooling rate of 0.3 K h^{-1} , which agrees with that shown in Bu et al. (2014). Another simulation
 331 using 625-m vertical grid spacing and RRTMG radiation produced 24-hour-average cooling rates
 332 of up to 0.6 K h^{-1} , which is consistent with the WRF simulations of Bu et al. (2014). This suggests
 333 that vertical grid spacing smaller than 625 m is necessary to resolve properly the radiative cooling

334 at the top of the cirrus canopy, and that the results can be quite sensitive to the radiation scheme
335 used.

336 Meanwhile below the tropopause, time-mean radiative warming spread from 30- to 160-km
337 radius within the cirrus canopy. The existence of radiative cooling overlying radiative warming in
338 this region led to radiatively-forced destabilization at and below the tropopause, as was observed
339 in Fig. 7d. Beneath the warming layer existed a region of forcing for stabilization, while a much
340 stronger region of forcing for stabilization existed in the lower stratosphere, above the cooling
341 maximum.

342 The results herein suggest that radiative heating tendencies played an important role in destabi-
343 lizing the upper troposphere and stabilizing the lower stratosphere after the cirrus canopy devel-
344 oped.

345 *c. The role of turbulent mixing*

346 Although vertical turbulence always acts to eliminate vertical gradients of θ , this adjustment
347 toward a neutral state only occurs where the mixing takes place. If turbulence occurs in a stably-
348 stratified layer, it will act to decrease θ at the top of the layer and increase it below. Just above and
349 just below the mixed layer, however, the θ profile remains undisturbed. Consequently, although
350 turbulent mixing acts to decrease $\partial\theta/\partial z$ in the layer in which it is occurring, it actually increases
351 $\partial\theta/\partial z$ just below and just above the layer. These vertical gradients of turbulent mixing are quite
352 important, particularly on the flanks of the upper-tropospheric outflow jet.

353 Two distinct maxima of vertical eddy diffusivity developed in the tropopause layer as the storm
354 intensified (Fig. 10). Comparison of these turbulent regions to the N^2 tendencies in Figs. 6c and
355 7c reveals that the layers in which vertical eddy diffusivity maximized corresponded to layers of
356 destabilization due to vertical turbulence. Just outside of these layers, however, vertical turbulence

acted to increase N^2 . The large vertical gradient of vertical eddy diffusivity near the tropopause played an important role in developing the lower-stratospheric stable layer during RI. This supports the hypothesized role of turbulence in setting the outflow-layer θ stratification in Rotunno and Emanuel (1987).

6. Conclusions

The simulated N^2 evolution shown herein closely matched that observed during the RI of Hurricane Patricia (2015). Three processes dominated the N^2 variability in the upper troposphere and lower stratosphere: advection, radiation, and vertical turbulence. Radiation and vertical turbulence played particularly important roles in developing the strong N^2 maximum just above the cold-point tropopause during RI. Since these two processes are parameterized, and radiation closely depends on yet another parameterized process (microphysics), the tropopause-layer N^2 variability could be quite sensitive to the assumptions inherent to the parameterizations used. A better understanding of the microphysical characteristics of the TC cirrus canopy, its interaction with radiation, and outflow-layer turbulence is critical to understanding the tropopause-layer N^2 evolution.

In this paper, all of the variables were averaged over a full diurnal cycle to eliminate the effects of diurnal variability and isolate the overall storm evolution. Diurnal variations in static stability near the tropopause are potentially of interest with respect to the tropical cyclone diurnal cycle, however, and will be the subject of future work.

Acknowledgments. We are indebted to George Bryan for his continued development and support of Cloud Model 1. We also thank Jeffrey Kepert, Robert Fovell, and Erika Navarro for helpful conversations related to this work. This research was supported by NSF Grant #1636799.

APPENDIX

Sensitivity experiments

The simulations exhibited some sensitivity to the initial thermodynamic profile and the prescribed vertical mixing length. Although the details of the intensification and the tropopause-layer N^2 evolution varied when these quantities were changed, the conclusions of the paper remain unchanged.

a. Sensitivity to the initial thermodynamic profile

A number of sensitivity experiments were conducted using a variety of initial soundings. Changing the initial temperature and humidity profiles affected the timing of the onset of organized deep convection and the rapidity of intensification. In all simulations, however, convection eventually penetrated to the tropopause, at which time vertical turbulence and radiation combined with advection to adjust the N^2 profile toward that which was observed in the control run. By the end of the RI period in every simulation, all three processes were actively modifying the N^2 profile near the tropopause.

As an example, 24-hour averages of N^2 are plotted in Fig. A1 for a simulation that was identical to that used in this paper, except the initial sounding was determined by averaging every CFSR grid point within 1000 km of TC Patricia's storm center at 18 UTC 21 October 2015 instead of averaging only within the 100-km radius. Although the lower-stratospheric stable layer developed more slowly and was weaker than that shown in Fig. 4, the overall evolution was quite similar and the same budget terms dominated the N^2 evolution.

b. Sensitivity to the vertical mixing length

The rate of turbulent mixing in the Smagorinsky scheme used herein is highly dependent on a prescribed length scale. The vertical mixing length used in this paper (100 m) was based on the

401 sensitivity experiments of Bryan (2012). Prescribing a smaller mixing length produces smaller
402 θ tendencies due to turbulence, but even with a mixing length on the low end of those tested
403 by Bryan (2012), turbulence still played an important role in the tropopause-layer N^2 evolution.
404 Fig. A2 shows the 24-hour-averaged contributions of turbulent mixing to the N^2 evolution from
405 a simulation identical to that used in this paper, except with a vertical mixing length of 50 m. At
406 all times, vertical turbulence still played an important role in the tropopause-layer N^2 evolution,
407 particularly during the latter stages of RI (48-72 hours).

408 References

- 409 Bryan, G. H., 2012: Effects of surface exchange coefficients and turbulence length scales on the
410 intensity and structure of numerically simulated hurricanes. *Mon. Wea. Rev.*, **140**, 1125–1143.
- 411 Bryan, G. H., cited 2018: The governing equations for CM1. [Available online at http://www2.mmm.ucar.edu/people/bryan/cm1/cm1_equations.pdf].
- 413 Bryan, G. H., and R. Rotunno, 2009: The maximum intensity of tropical cyclones in axisymmetric
414 numerical model simulations. *Mon. Wea. Rev.*, **137**, 1770–1789.
- 415 Bu, Y. P., R. G. Fovell, and K. L. Corbosiero, 2014: Influence of cloud-radiative forcing on tropical
416 cyclone structure. *J. Atmos. Sci.*, **71**, 1644–1622.
- 417 Doyle, J. D., and Coauthors, 2017: A view of tropical cyclones from above: The Tropical Cyclone
418 Intensity (TCI) Experiment. *Bull. Amer. Meteor. Soc.*, **98**, 2113–2134.
- 419 Duran, P., and J. Molinari, 2018: Dramatic inner-core tropopause variability during the rapid
420 intensification of Hurricane Patricia (2015). *Mon. Wea. Rev.*, **146**, 119–134.
- 421 Emanuel, K., 2012: Self-stratification of tropical cyclone outflow. Part II: Implications for storm
422 intensification. *J. Atmos. Sci.*, **69**, 988–996.

423 Emanuel, K., and R. Rotunno, 2011: Self-stratification of tropical cyclone outflow. Part I: Impli-
 424 cations for storm structure. *J. Atmos. Sci.*, **68**, 2236–2249.

425 Iacono, M. J., J. S. Delamere, E. J. Mlawer, M. W. Shephard, S. A. Clough, and W. D. Collins,
 426 2008: Radiative forcing by long-lived greenhouse gases: Calculations with the AER radiative
 427 transfer models. *J. Geophys. Res.*, **113** (D13103).

428 Kepert, J. D., J. Schwendike, and H. Ramsay, 2016: Why is the tropical cyclone boundary layer
 429 not ”well mixed”? *J. Atmos. Sci.*, **73**, 957–973.

430 Kieu, C., V. Tallapragada, D.-L. Zhang, and Z. Moon, 2016: On the development of double warm-
 431 core structures in intense tropical cyclones. *J. Atmos. Sci.*, **73**, 4487–4506.

432 Kimberlain, T. B., E. S. Blake, and J. P. Cangialosi, 2016: Tropical cyclone report: Hurricane
 433 Patricia. National Hurricane Center. [Available online at www.nhc.noaa.gov].

434 Komaromi, W. A., and J. D. Doyle, 2017: Tropical cyclone outflow and warm core structure as
 435 revealed by HS3 dropsonde data. *Mon. Wea. Rev.*, **145**, 1339–1359.

436 Markowski, P. M., and G. H. Bryan, 2016: LES of laminar flow in the PBL: A potential problem
 437 for convective storm simulations. *Mon. Wea. Rev.*, **144**, 1841–1850.

438 Ohno, T., and M. Satoh, 2015: On the warm core of a tropical cyclone formed near the tropopause.
 439 *J. Atmos. Sci.*, **72**, 551–571.

440 Rogers, R. F., S. Aberson, M. M. Bell, D. J. Cecil, J. D. Doyle, J. Morgerman, L. K. Shay, and
 441 C. Velden, 2017: Re-writing the tropical record books: The extraordinary intensification of
 442 Hurricane Patricia (2015). *Bull. Amer. Meteor. Soc.*, **98**, 2091–2112.

443 Rotunno, R., and K. A. Emanuel, 1987: An air-sea interaction theory for tropical cyclones. Part II:
444 Evolutionary study using a nonhydrostatic axisymmetric numerical model. *J. Atmos. Sci.*, **44**,
445 542–561.

446 Stern, D. P., and F. Zhang, 2013: How does the eye warm? Part I: A potential temperature budget
447 analysis of an idealized tropical cyclone. *J. Atmos. Sci.*, **70**, 73–89.

448 Thompson, G., R. M. Rasmussen, and K. Manning, 2004: Explicit forecasts of winter precipitation
449 using an improved bulk microphysics scheme. Part I: Description and sensitivity analysis. *Mon.*
450 *Wea. Rev.*, **132**, 519–542.

451 Trier, S. B., and R. D. Sharman, 2009: Convection-permitting simulations of the environment sup-
452 porting widespread turbulence within the upper-level outflow of a mesoscale convective system.
453 *Mon. Wea. Rev.*, **137**, 1972–1990.

454 LIST OF FIGURES

- 455 **Fig. 1.** The maximum 10-m wind speed (top panel; m s^{-1}) and minimum sea-level pressure (bottom
456 panel; hPa) in the simulated storm (blue lines; plotted every minute) and from Hurricane
457 Patricia's best track (red stars; plotted every six hours beginning at the time Patricia attained
458 tropical storm intensity). The rapid weakening during the later stage of Patricia's lifetime
459 was induced by landfall. 26
- 460 **Fig. 2.** Left panels: Twenty-four-hour changes in squared Brunt-Väisälä frequency (N^2 ; 10^{-4} s^{-2})
461 computed using Eq. 8 over (top row) 0-24 hours, (middle row) 24-48 hours, (bottom row)
462 48-72 hours. Middle Panels: The N^2 change over the same time periods computed using Eqs.
463 4-7, Right Panels: The budget residual over the same time periods, computed by subtracting
464 the budget change (middle column) from the model change (left column). Orange lines
465 represent the cold-point tropopause height averaged over the same time periods. 27
- 466 **Fig. 3.** Time series of the contribution of each of the budget terms to the time tendency of the
467 squared Brunt-Väisälä frequency (N^2 ; 10^{-4} s^{-2}). For each budget term, the absolute value
468 of the N^2 tendency is averaged temporally over 1-hour periods (using output every minute),
469 and spatially in a region extending from 0 to 200 km radius and 14 to 21 km altitude. 28
- 470 **Fig. 4.** Twenty-four-hour averages of squared Brunt-Väisälä frequency (N^2 ; 10^{-4} s^{-2}) over (a) 0-24
471 hours, (b) 24-48 hours, (c) 48-72 hours. Orange lines represent the cold-point tropopause
472 height averaged over the same time periods. 29
- 473 **Fig. 5.** (a) Total change in N^2 over the 0-24-hour period ($10^{-4} \text{ s}^{-2} (24 \text{ h})^{-1}$) and the contributions to
474 that change from (b) the sum of horizontal and vertical advection, (c) vertical turbulence, (d)
475 longwave and shortwave radiation, (e) the sum of horizontal advection, vertical advection,

476	and vertical turbulence, and (f) the sum of horizontal advection, vertical advection, vertical	
477	turbulence, and longwave and shortwave radiation. Orange lines represent the cold-point	
478	tropopause height averaged over the 0-24-hour period.	31
479	Fig. 6. As in Fig. 5, but for the 24-48-hour period.	32
480	Fig. 7. As in Fig. 5, but for the 48-72-hour period.	33
481	Fig. 8. The contributions to the change in N^2 over the 24-48-hour period ($10^{-4} \text{ s}^{-2} (24 \text{ h})^{-1}$) by	
482	(a) horizontal advection and (b) vertical advection. (c) The radial velocity (m s^{-1} ; filled con-	
483	tours), potential temperature (K; thick black contours), cold-point tropopause height (orange	
484	line), and level of maximum outflow (dashed cyan line) averaged over the 24-48-hour period.	
485	(d) The vertical velocity (cm s^{-1} ; filled contours), potential temperature (K; thick black con-	
486	tours), and cold-point tropopause height (orange line) averaged over the 24-48-hour period.	
487	34	
488	Fig. 9. Ice mixing ratio (g kg^{-1}) and cold-point tropopause height (orange lines) averaged over (a)	
489	0-24 hours, (c) 24-48 hours, and (e) 48-72 hours. Radiative heating rate (K h^{-1}) and cold-	
490	point tropopause height (orange lines) averaged over (b) 0-24 hours, (d) 24-48 hours, and (f)	
491	48-72 hours.	36
492	Fig. 10. Vertical eddy diffusivity ($\text{m}^2 \text{ s}^{-2}$; filled contours), cold-point tropopause height (cyan lines),	
493	and radial velocity (m s^{-1} ; thick black lines) averaged over (a) 0-24 hours, (b) 24-48 hours,	
494	and (c) 48-72 hours.	37
495	Fig. A1. Twenty-four-hour averages of squared Brunt-Väisälä frequency (N^2 ; 10^{-4} s^{-2}) over (a) 0-24	
496	hours, (b) 24-48 hours, (c) 48-72 hours, and (d) 72-96 hours for the simulation described	

in Appendix Aa. Orange lines represent the cold-point tropopause height averaged over the same time periods. 38

Fig. A2. The contribution of vertical turbulence to the N^2 variability ($10^{-4} \text{ s}^{-2} (24 \text{ h})^{-1}$) averaged over (a) 0-24 hours, (b) 24-48 hours, (c) 48-72 hours, and (d) 72-96 hours for the simulation described in Appendix Ab. Orange lines represent the cold-point tropopause height averaged over the same time periods. 39

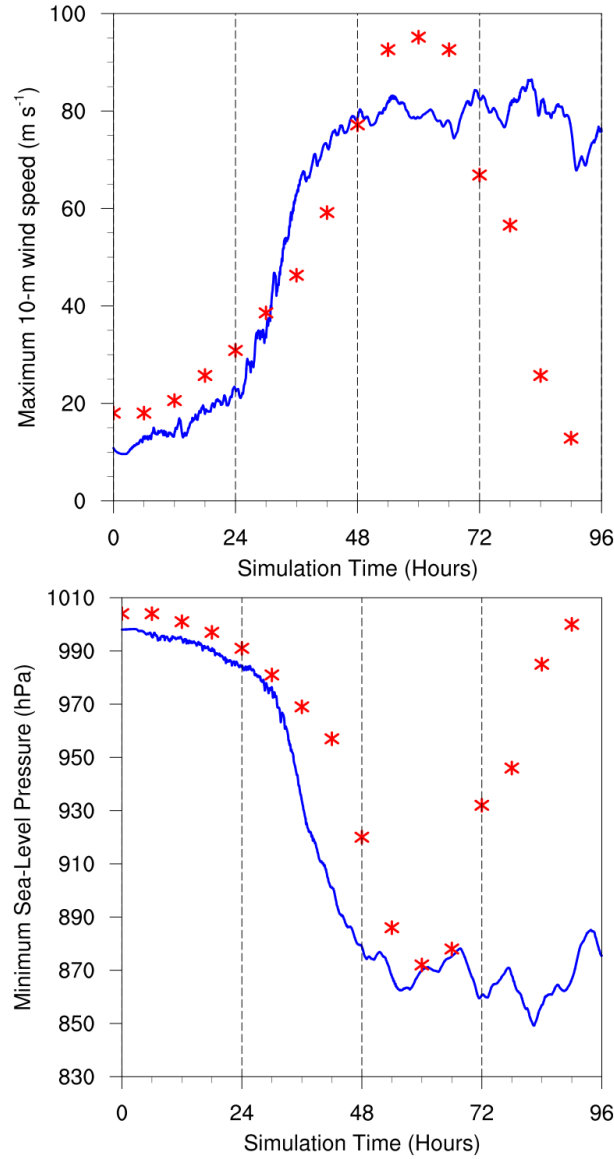


FIG. 1. The maximum 10-m wind speed (top panel; m s^{-1}) and minimum sea-level pressure (bottom panel; hPa) in the simulated storm (blue lines; plotted every minute) and from Hurricane Patricia's best track (red stars; plotted every six hours beginning at the time Patricia attained tropical storm intensity). The rapid weakening during the later stage of Patricia's lifetime was induced by landfall.

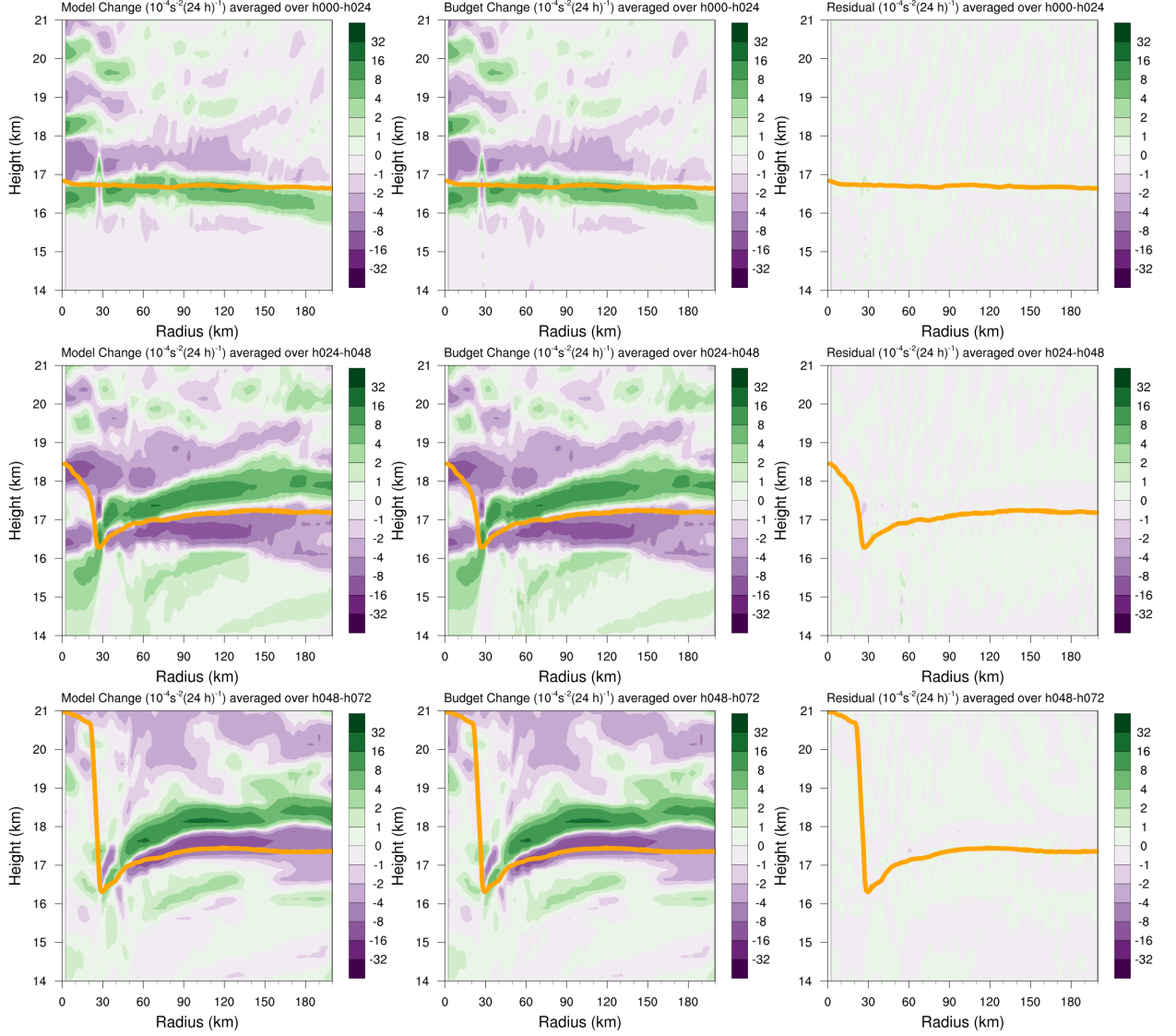


FIG. 2. Left panels: Twenty-four-hour changes in squared Brunt-Väisälä frequency (N^2 ; 10^{-4} s^{-2}) computed using Eq. 8 over (top row) 0-24 hours, (middle row) 24-48 hours, (bottom row) 48-72 hours. Middle Panels: The N^2 change over the same time periods computed using Eqs. 4-7, Right Panels: The budget residual over the same time periods, computed by subtracting the budget change (middle column) from the model change (left column). Orange lines represent the cold-point tropopause height averaged over the same time periods.

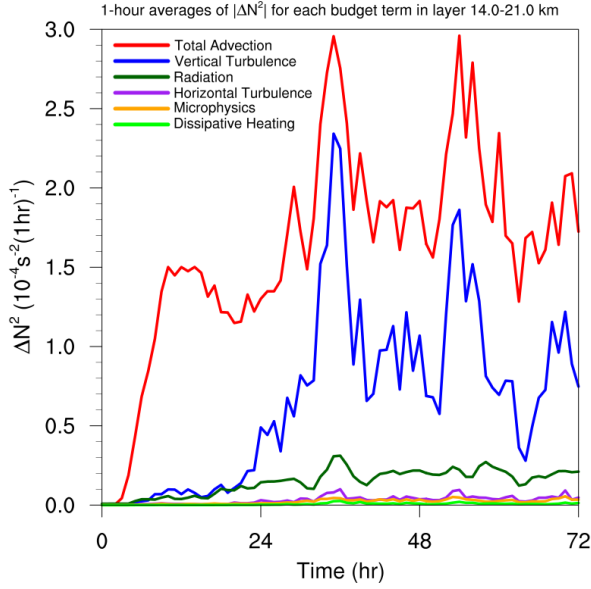
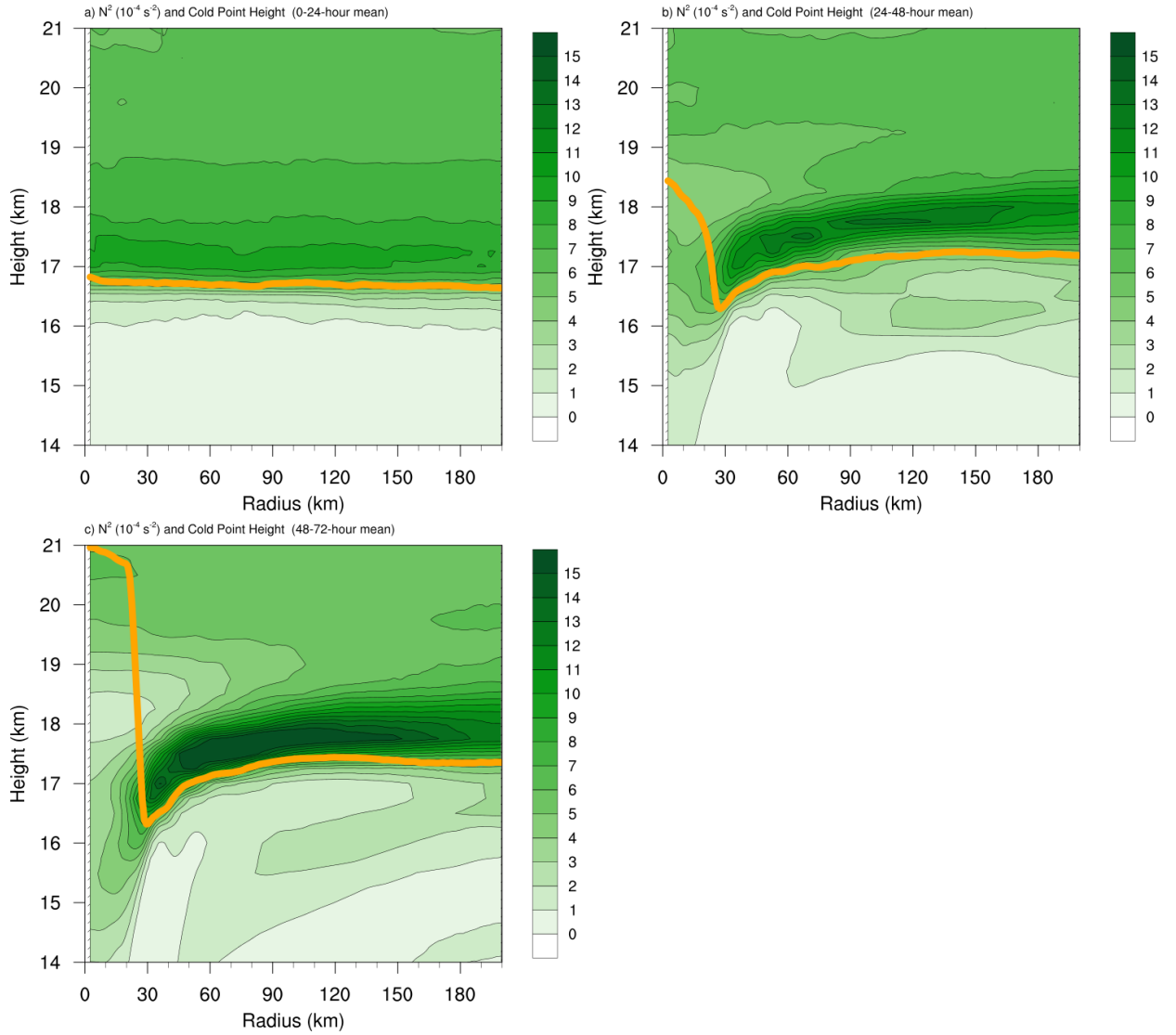
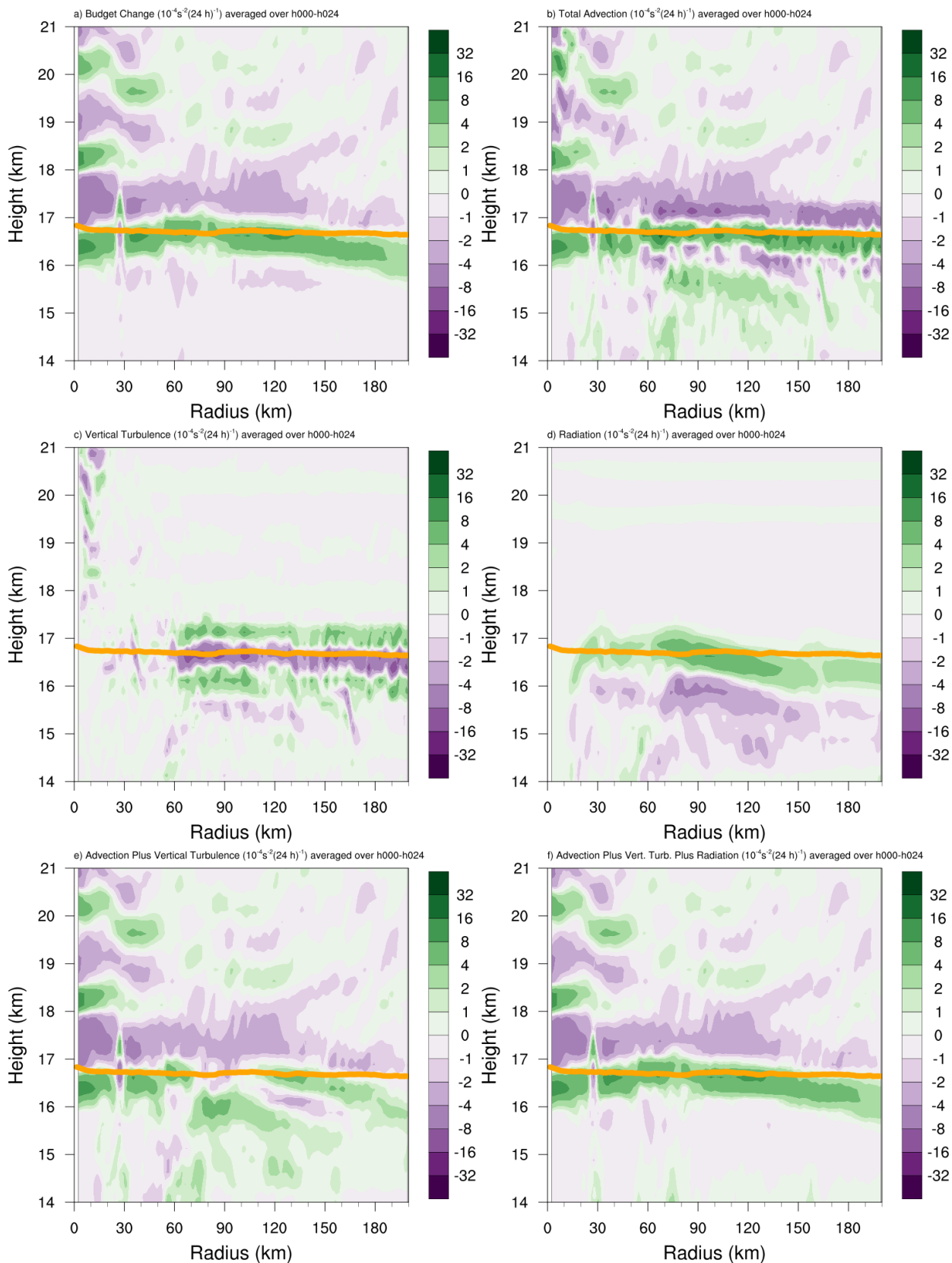


FIG. 3. Time series of the contribution of each of the budget terms to the time tendency of the squared Brunt-Väisälä frequency (N^2 ; 10^{-4} s^{-2}). For each budget term, the absolute value of the N^2 tendency is averaged temporally over 1-hour periods (using output every minute), and spatially in a region extending from 0 to 200 km radius and 14 to 21 km altitude.



516 FIG. 4. Twenty-four-hour averages of squared Brunt-Väisälä frequency (N^2 ; 10^{-4} s^{-2}) over (a) 0-24 hours, (b)
 517 24-48 hours, (c) 48-72 hours. Orange lines represent the cold-point tropopause height averaged over the same
 518 time periods.



519 FIG. 5. (a) Total change in N^2 over the 0-24-hour period ($10^{-4} \text{ s}^{-2} (24 \text{ h})^{-1}$) and the contributions to that change
520 from (b) the sum of horizontal and vertical advection, (c) vertical turbulence, (d) longwave and shortwave
521 radiation, (e) the sum of horizontal advection, vertical advection, and vertical turbulence, and (f) the sum of
522 horizontal advection, vertical advection, vertical turbulence, and longwave and shortwave radiation. Orange
523 lines represent the cold-point tropopause height averaged over the 0-24-hour period.

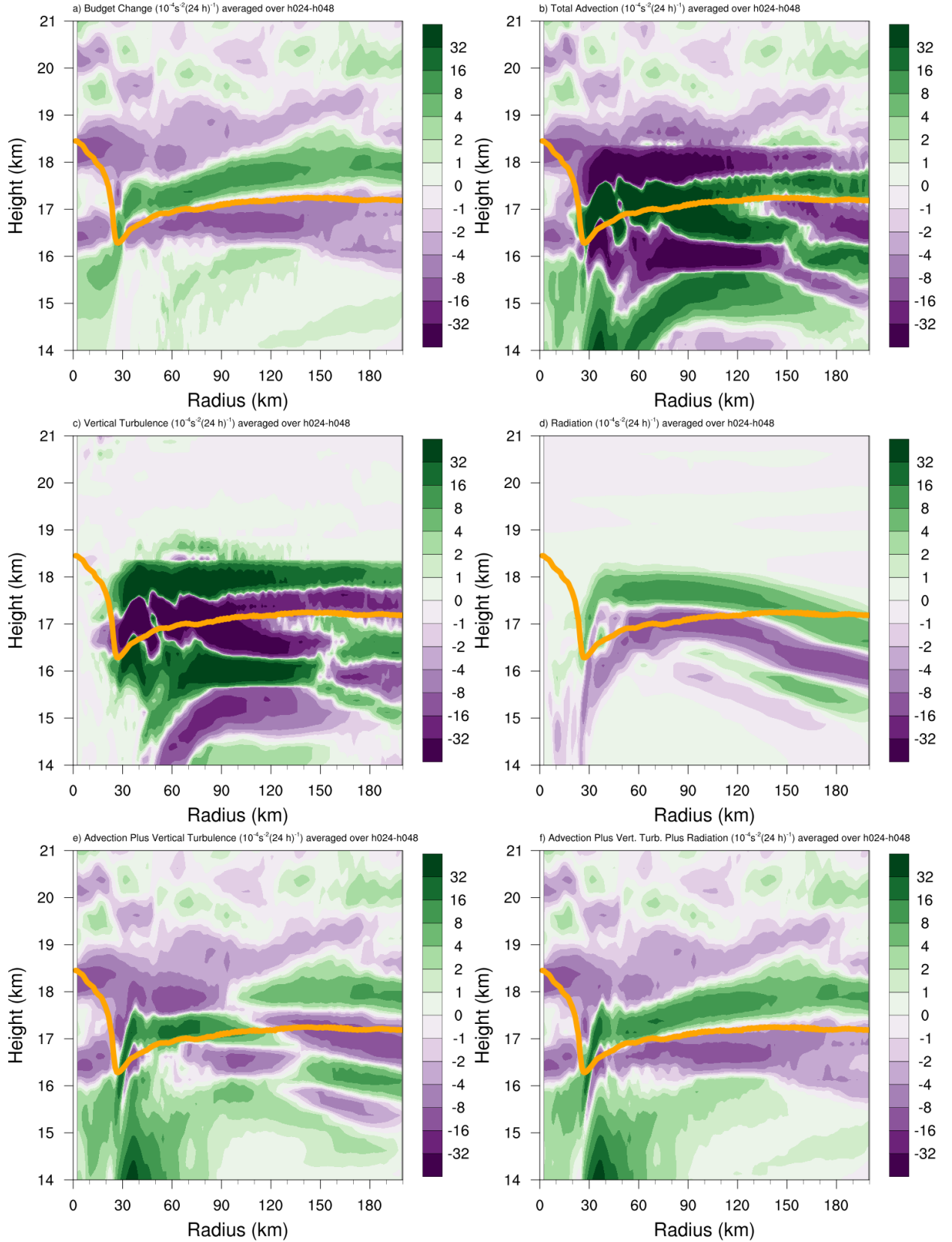


FIG. 6. As in Fig. 5, but for the 24-48-hour period.

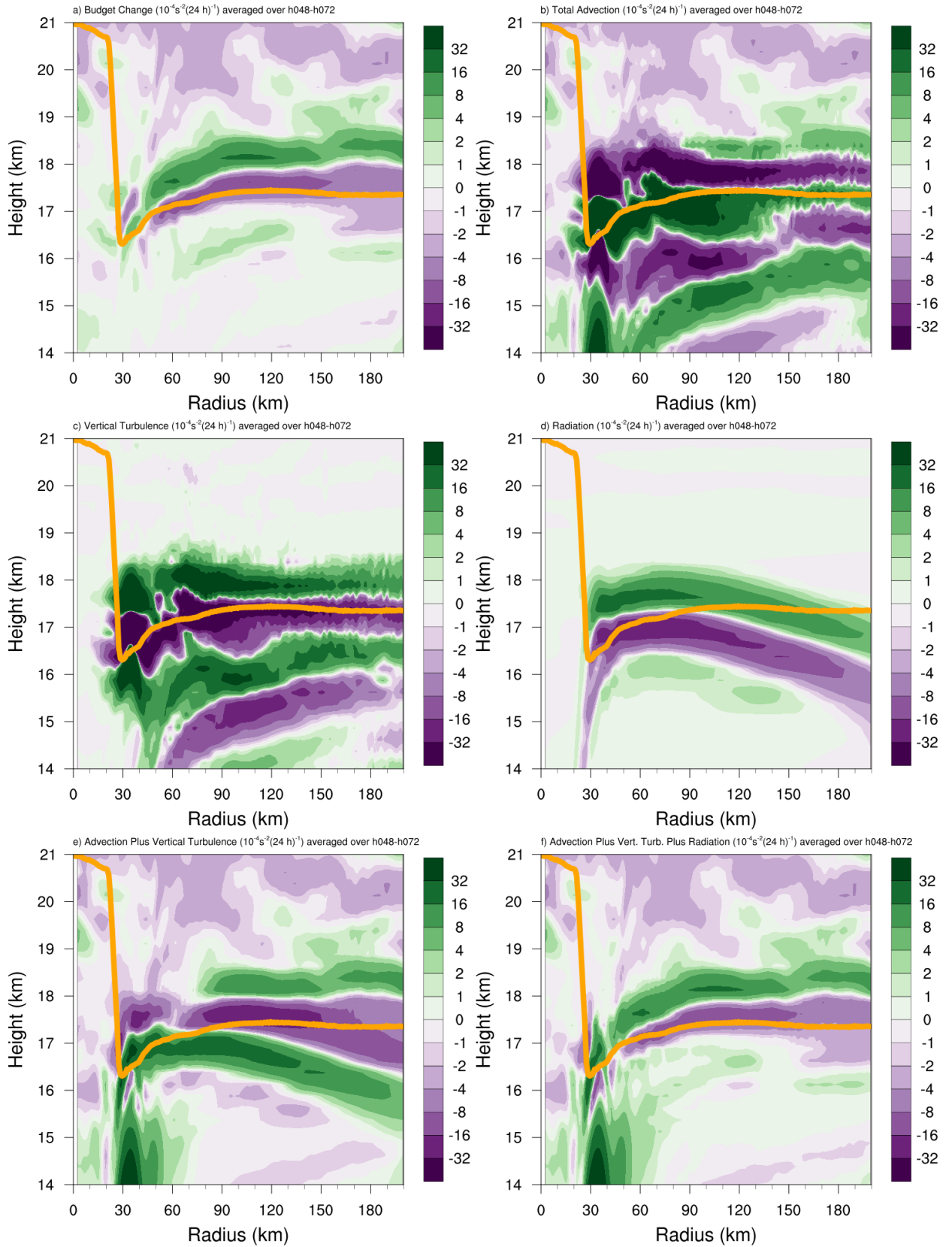


FIG. 7. As in Fig. 5, but for the 48-72-hour period.

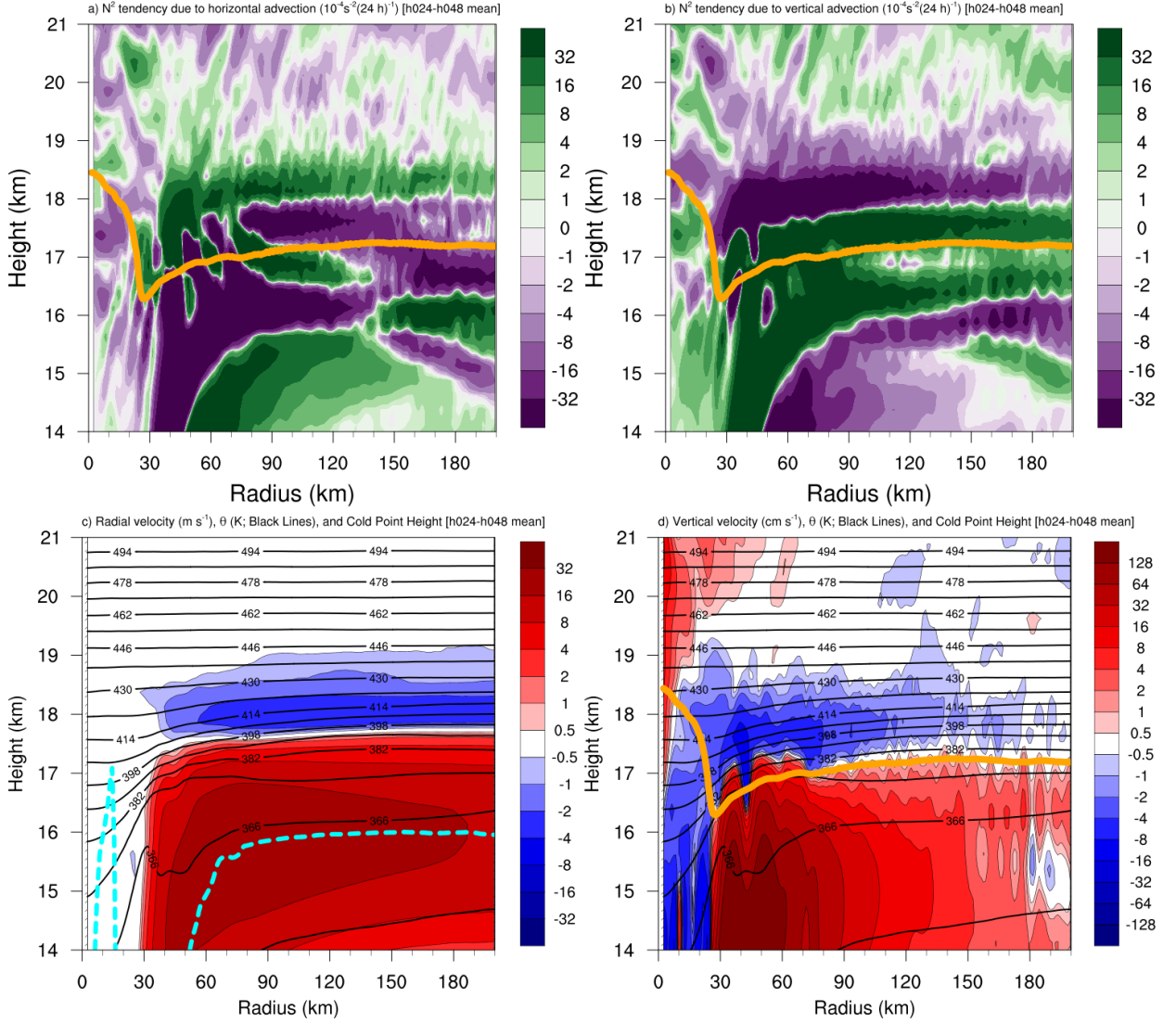
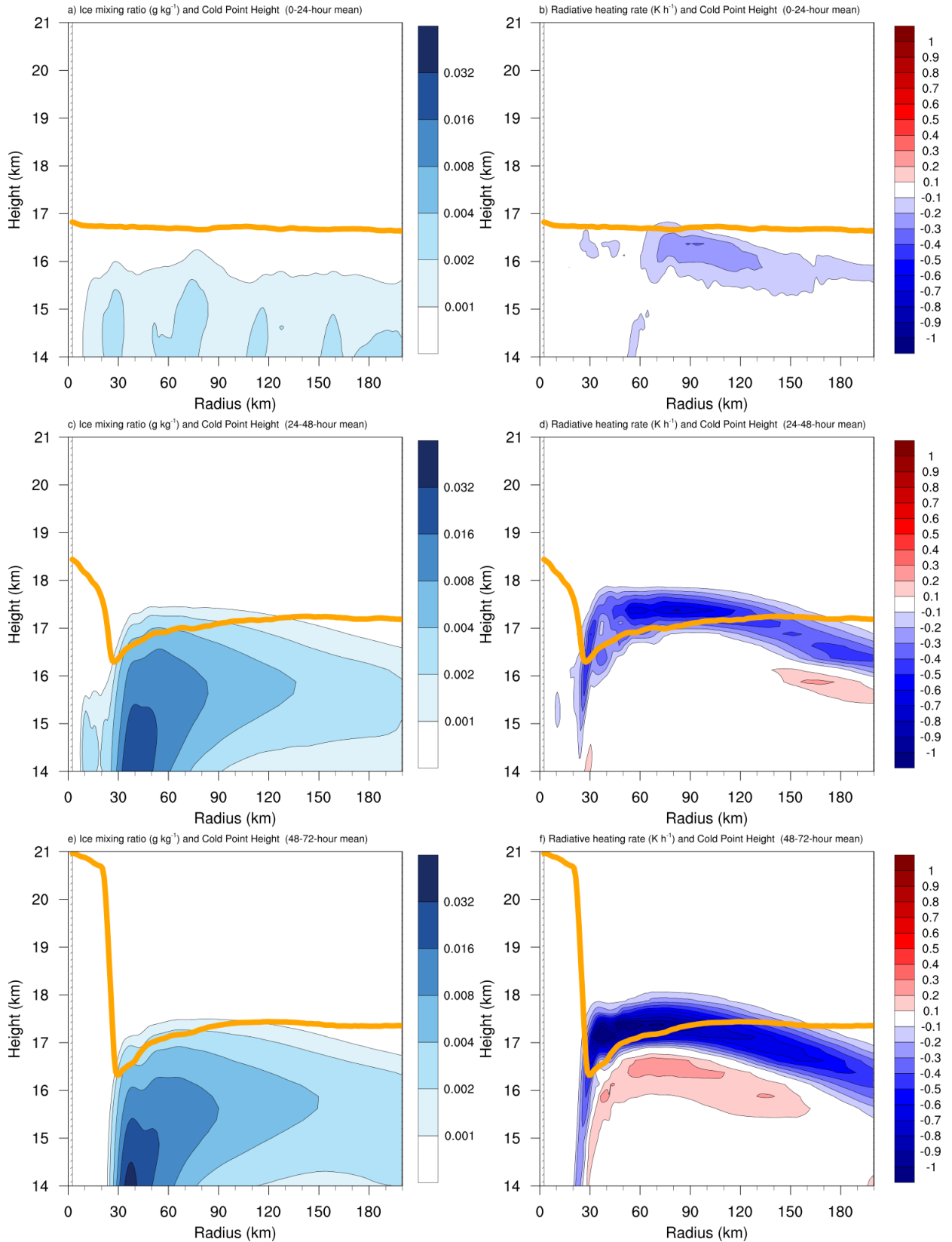


FIG. 8. The contributions to the change in N^2 over the 24-48-hour period ($10^{-4} \text{ s}^{-2} (24 \text{ h})^{-1}$) by (a) horizontal advection and (b) vertical advection. (c) The radial velocity (m s^{-1} ; filled contours), potential temperature (K; thick black contours), cold-point tropopause height (orange line), and level of maximum outflow (dashed cyan line) averaged over the 24-48-hour period. (d) The vertical velocity (cm s^{-1} ; filled contours), potential temperature (K; thick black contours), and cold-point tropopause height (orange line) averaged over the 24-48-hour period.



530 FIG. 9. Ice mixing ratio (g kg^{-1}) and cold-point tropopause height (orange lines) averaged over (a) 0-24 hours,
531 (c) 24-48 hours, and (e) 48-72 hours. Radiative heating rate (K h^{-1}) and cold-point tropopause height (orange
532 lines) averaged over (b) 0-24 hours, (d) 24-48 hours, and (f) 48-72 hours.

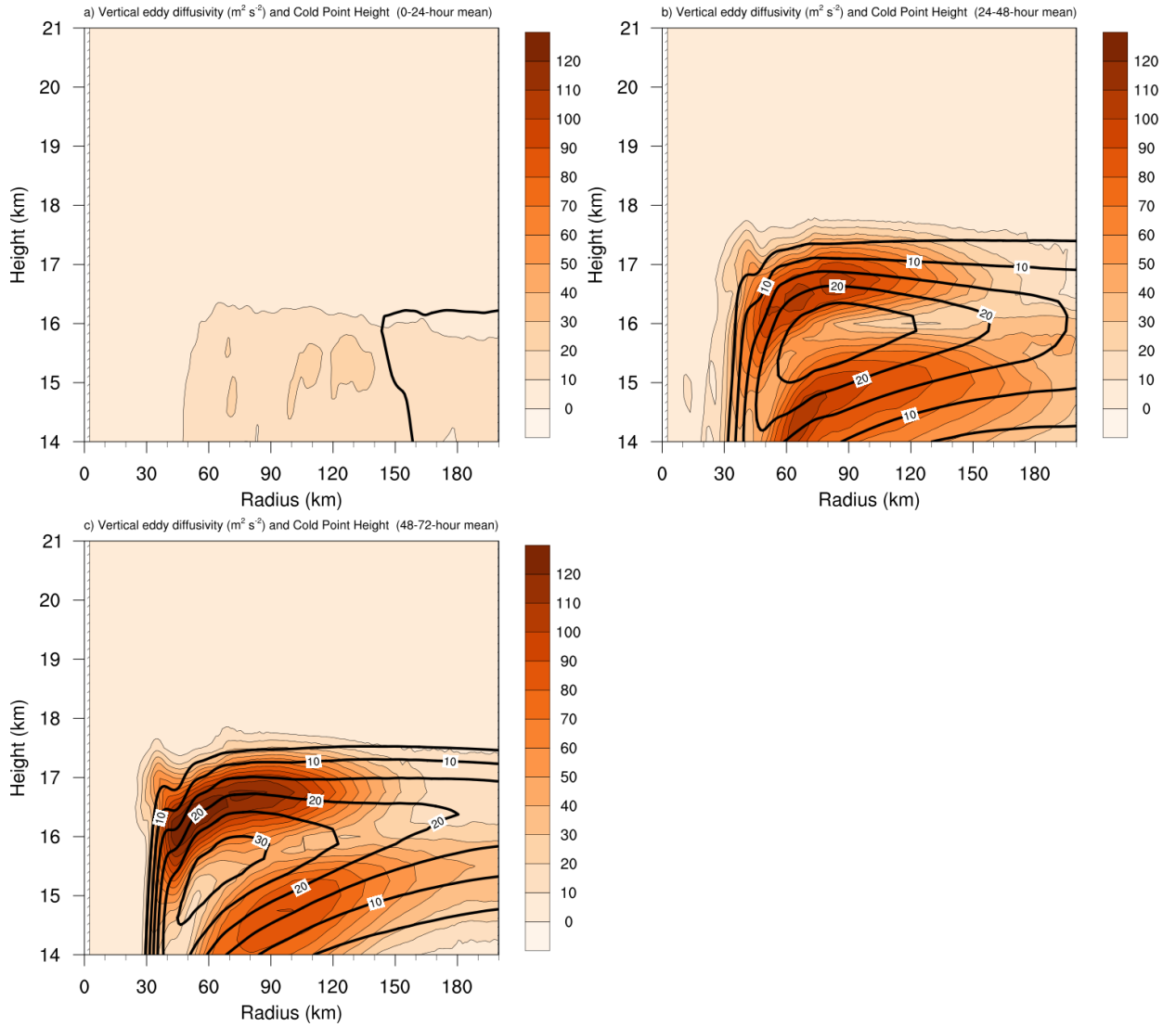
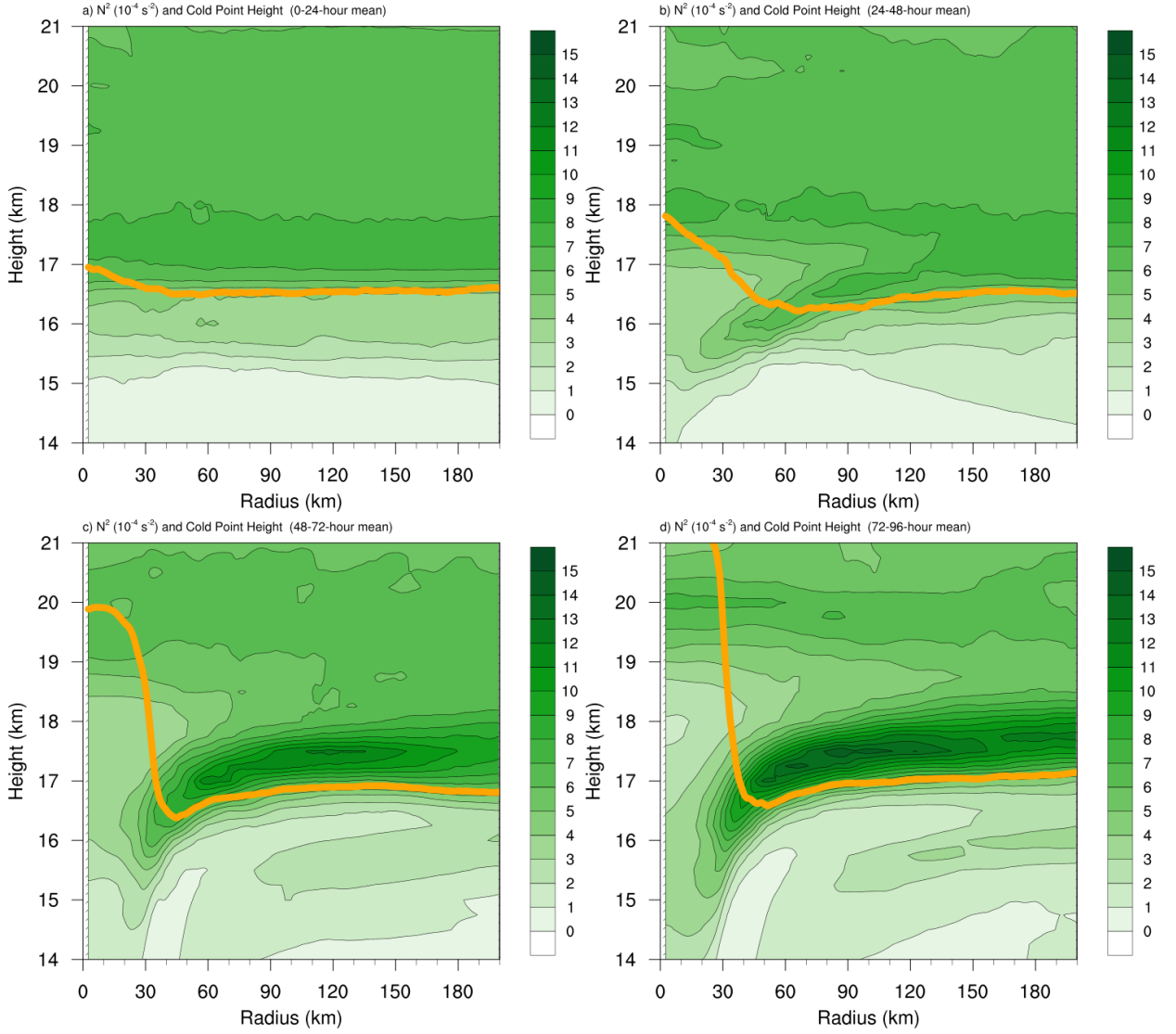


FIG. 10. Vertical eddy diffusivity ($\text{m}^2 \text{s}^{-2}$; filled contours), cold-point tropopause height (cyan lines), and radial velocity (m s^{-1} ; thick black lines) averaged over (a) 0-24 hours, (b) 24-48 hours, and (c) 48-72 hours.



535 Fig. A1. Twenty-four-hour averages of squared Brunt-Väisälä frequency (N^2 ; 10^{-4} s^{-2}) over (a) 0-24 hours,
 536 (b) 24-48 hours, (c) 48-72 hours, and (d) 72-96 hours for the simulation described in Appendix Aa. Orange lines
 537 represent the cold-point tropopause height averaged over the same time periods.

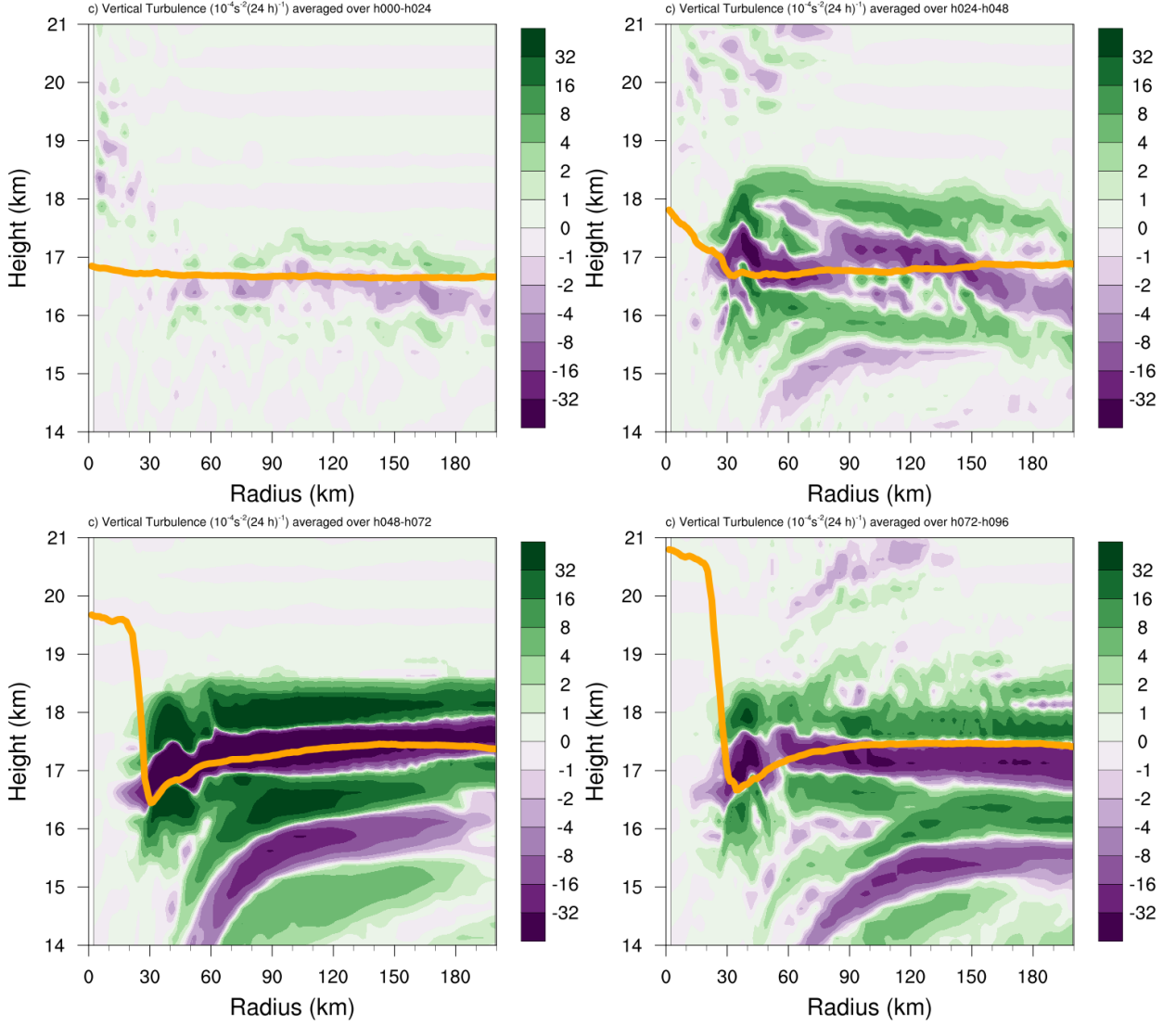


Fig. A2. The contribution of vertical turbulence to the N^2 variability ($10^{-4} \text{ s}^{-2} (24 \text{ h})^{-1}$) averaged over (a) 0-24 hours, (b) 24-48 hours, (c) 48-72 hours, and (d) 72-96 hours for the simulation described in Appendix Ab. Orange lines represent the cold-point tropopause height averaged over the same time periods.